Iranian Journal of Medical Physics

ijmp.mums.ac.ir

Design and Biodistribution of ^{99m}Tc-Labeled Gold/Gold Sulfide Nanoconjugates: A Preclinical Evaluation in Balb/c Mice

Esmat Ramezanzadeh[1,2], Mohammad Hossein Bahreyni Toosi[1,2], Ameneh Sazgarnia[1,2], Kayvan Sadri[3*]

1. Department of Medical Physics, Faculty of Medicine, Mashhad University of Medical Sciences, Mashhad, Iran
2. Medical Physics Research Center, Basic Sciences Research Institute, Mashhad University of Medical Sciences, Mashhad, Iran
3. Nuclear Medicine Research Center, Mashhad University of Medical Sciences, Mashhad, Iran

ARTICLE INFO

Article type:
Original Paper

Article history:
Received: Jul 12, 2025
Accepted: Nov 10, 2025

Keywords:
Nanoparticles
Gold/Gold Sulfide
Biodistribution
Technetium Tc 99m

ABSTRACT

Introduction: Gold/gold sulfide (GGS) nanoparticles exhibit strong near-infrared (NIR) absorption, high chemical stability, low cytotoxicity, and ease of surface functionalization, enabling deep tissue penetration and targeted cancer theranostics. This study aimed to develop and evaluate ^{99m}Tc-labeled PEGylated GGS nanoconjugates for potential SPECT imaging applications.

Material and Methods: GGS nanoparticles were synthesized by reacting $HAuCl_4$ with Na_2S and stabilized with polyvinylpyrrolidone (PVP). PEGylated GGS nanoparticles were radiolabeled with ^{99m}Tc using $SnCl_2$, and radiochemical purity and stability were assessed via ITLC in RPMI and human serum up to 24 h. Cytotoxicity and cellular uptake were evaluated in CT26 colon carcinoma cells. Biodistribution was studied in BALB/c mice at 1, 4, and 24h post-intravenous injection by gamma counting of excised organs.

Results: ^{99m}Tc-GGS-PVP nanoconjugates had an average diameter of ~65.9 nm, maintained strong NIR absorption post-labeling, and achieved high radiochemical purity (97.1 ± 1.1%) with stability >85% in RPMI and >82% in human serum at 24h. Cytotoxicity was minimal, with 78% cell viability at 125 μmol GGS. Cellular uptake increased from 1.98% at 2h to 10.0% at 24h. In vivo, the liver showed the highest uptake (51.44 ± 7.54 %ID/g at 1h), decreasing to 14.19 ± 6.54 %ID/g at 24h; spleen uptake was markedly lower (1.51 ± 0.81 %ID/g at 1h, 0.765 ± 0.28 %ID/g at 24h).

Conclusion: The synthesized ^{99m}Tc-GGS-PVP nanoparticles demonstrated high stability, low toxicity, favorable biodistribution, and preserved NIR absorption properties, making them promising candidates for dual-modality cancer theranostics. Their radiolabeling efficiency and biodistribution support their use as radiotracers for SPECT imaging and potential integration into combined diagnostic and therapeutic (theranostic) platforms.

►*Please cite this article as:*
Ramezanzadeh E, Bahreyni Toosi MH, Sazgarnia A, Sadri K. Design and Biodistribution of ^{99m}Tc-Labeled Gold/Gold Sulfide Nanoconjugates: A Preclinical Evaluation in Balb/c Mice. Iran J Med Phys 2025; 22: 230-240. 10.22038/ijmp.2025.89531.2580.

Introduction

Although cancer treatments have progressed significantly, achieving selective tumor targeting while avoiding damage to healthy tissues remains challenging. Gold nanoparticles have emerged as promising theranostic agents due to their tunable near-infrared (NIR) absorption, which enables deep tissue penetration for both imaging and therapy.

This property enables deep tissue penetration while minimizing collateral damage, making NIR-responsive nanostructures highly suitable for noninvasive applications such as targeted imaging and localized thermal therapies [1-4]. Gold nanoparticles can rapidly convert absorbed NIR light into heat, raising local temperatures by over 10°C within nanoseconds [3], a feature beneficial for photothermal [5] and hyperthermia-based treatments [4]. These effects are largely attributed to localized surface plasmon resonance (LSPR) [2, 6, 7], which also allows for easy surface functionalization. As a result, gold nanostructures are promising candidates for multifunctional platforms capable of simultaneous imaging and therapy.

Various gold nanoparticle platforms have been explored, including silica-based nanoshells [2, 3, 8, 9], gold nanorods [10], nanospheres [11], and nanocages [12]. Gold nanorods offer adjustable plasmon peaks but can suffer from reduced chemical stability and potential shape-dependent cytotoxicity [13]. Silica-based nanoshells exhibit strong photothermal effects but typically require larger particle sizes (~100–150 nm), which may limit tumor penetration [14]. In contrast, gold/gold sulfide (GGS) nanoparticles combine strong NIR absorption around 800 nm with smaller size ranges (~35–65 nm), enhanced chemical stability, low inherent cytotoxicity, their distinctive physicochemical advantage, and cost-effective synthesis. These advantages position GGS nanoparticles as highly promising candidates for

*Corresponding Author: Tel: +98 05138012783; E-mail: sadrik@mums.ac.ir

multifunctional theranostic platforms capable of simultaneous imaging and targeted therapy [3].

GGS nanoparticles feature a gold core surrounded by a thin gold sulfide shell that not only enhances optical absorption within the NIR window, but also improves thermal performance. [3, 8]. Their smaller size facilitates deeper tissue penetration, while their superior chemical stability and tunable morphology support long-term colloidal stability [1, 3, 8]. Moreover, GGS nanoparticles can be readily functionalized with targeting ligands such as antibodies [1, 3], peptides [15], or anticancer agents to improve tumor selectivity and therapeutic efficacy across modalities including photothermal therapy [2, 3], hyperthermia [4], and photoimmunotherapy [16, 17]. When coated with stabilizers like polyvinylpyrrolidone (PVP), they demonstrate excellent biocompatibility and reduced systemic toxicity [1, 3, 15]. These combined attributes position GGS nanoparticles as strong candidates for next-generation integrated diagnostic and therapeutic (theranostic) systems, especially in advanced light-triggered cancer treatments [16].

Based on extensive studies conducted on gold/gold sulfide nanoparticles, these nanostructures have gained attention as multifunctional platforms for therapeutic and diagnostic applications. Gobin et al. [2] showed that 35–55 nm GGS nanoparticles had superior optical absorption and tumor penetration compared to gold/silica nanoshells, resulting in a marked increase in long-term tumor-free survival in animal models. Day et al. [18] demonstrated their dual functionality in two-photon microscopy and thermal ablation, particularly when conjugated with anti-HER2 antibodies to target SK-BR-3 breast cancer cells.

Darbandi and colleagues [4, 9] found that GGS nanoparticles, with an IC50 of around 350 μmol in MCF-7 cells, exhibited lower toxicity and significantly enhanced the effectiveness of combined hyperthermia and radiotherapy. Demir et al. [8] successfully synthesized stable variants of GGS nanoparticles with various anionic, cationic, and protein coatings that demonstrated remarkable photoacoustic activity in both visible (532 nm) and NIR (800 nm) regions, outperforming spherical gold nanoparticles and showing comparable efficacy to nanorods. Additionally, Banihashem et al. [19] also developed chitosan-grafted poly nanofibers coated with GGS nanoparticles for controlled cisplatin release, showing promising effects in treating MCF-7 cells. Despite their therapeutic promise, the in vitro stability and in vivo biodistribution of radiolabeled GGS nanoparticles remain largely unexplored, highlighting the need for systematic pharmacokinetic studies.

In response to this gap, the present study was designed to develop technetium-99m (^{99m}Tc)-labeled PEGylated GGS nanoconjugates and investigate their radiochemical stability in biological media along with their biodistribution in BALB/c mice. The strong NIR absorption, high chemical stability, low cytotoxicity, and excellent surface functionalization potential make GGS nanoparticles highly suitable for radiolabeling with ^{99m}Tc. While these nanostructures hold promise for future theragnostic applications, including combined imaging and thermal therapies, the current work is focused specifically on characterizing their pharmacokinetic behavior and tissue distribution. PEGylation is expected to prolong systemic circulation and improve passive targeting via the enhanced permeability and retention (EPR) effect. Accordingly, this study presents foundational data on the biological behavior of ^{99m}Tc-GGS-PVP nanoconjugates to inform their potential development as radiotracers for future SPECT applications.

Materials and Methods

GGS-NP and ^{99m}Tc –GGS-PVP synthesis

GGS-Np synthesis and characterization

Au-AuS nanoparticles were synthesized via a controlled reaction between aqueous solutions of $HAuCl_4$ (Alfa Aesar, USA) and Na_2S (Merck, Germany). The synthesis procedure involved combining 20 mL of 2 mM $HAuCl_4$ with 20 mL of 1 mM Na_2S in a reaction vessel, followed by incubation at 25°C for 24 hours to allow complete formation of the nanostructures. The reaction progress was monitored using a UV-visible spectrophotometer (UV 1700, Shimadzu Corp., Japan) across the wavelength range of 200-900 nm to confirm the characteristic spectral signature of the GGS nanoparticles. To enhance colloidal stability and prevent aggregation, 0.6 gr of polyvinylpyrrolidone (PVP; (C_6H_9NO) n) was added to the nanoparticle suspension as a stabilizing agent. The resulting GGS-PVP nanoshells were subsequently purified through a sequential centrifugation procedure to remove unreacted precursors and excess stabilizing agents, yielding a homogeneous suspension of well-dispersed nanoparticles [2, 20]. Finally, purified GGS nanoshells were obtained through a systematic sequential centrifugation process and the particle size analyzer (Zetasizer, Malvern Inc., USA) was used to the size distribution of the nanoparticles.

^{99m}Tc-GGS-PVP nanoconjugate synthesis and characterization

For radiolabeling of GGS-PVP nanoparticles, Technetium-99m (^{99m}Tc) with a radioactivity of 10 mCi was utilized as the radiotracer. The ^{99m}Tc was eluted from a generator using distilled water (rather than the conventional normal saline) and collected in a sterile, evacuated vial (5 mL volume). For radiolabeling of GGS-PVP nanoparticles with ^{99m}Tc, we first optimized the reducing agent preparation by dissolving 1 mg $SnCl_2$ in 1 mL of 0.1N HCl and stirring vigorously for 1 minute to ensure complete dissolution. This step is critical for effective reduction of ^{99m}Tc and subsequent attachment to the nanoparticle surface. The radiolabeling procedure was performed in a sterile glass vial where 5 mL of the GGS-PVP nanoparticle solution

was mixed with 1 mL of freshly eluted ^{99m}Tc (10 mCi) obtained using distilled water rather than conventional normal saline. This modification was specifically implemented after preliminary experiments showed that distilled water elution significantly enhanced labeling efficiency by reducing competing ions during the radiolabeling process. Above mixture was then incubated for 10 minutes on a laboratory tube rocker at medium speed (approximately 20-25 rpm) at room temperature (25°C).

To ensure high radiochemical purity, the mixture containing ^{99m}Tc-GGS-PVP nanoconjugate was purified using a Sephadex G25 column chromatography, which effectively separated the radiolabeled nanoconjugate from free (unconjugated) ^{99m}Tc. (Figure 3)

The final ^{99m}Tc-GGS-PVP nanoconjugates were characterized for size distribution using dynamic light scattering (Zetasizer, Malvern Inc., USA). Additionally, UV-visible spectroscopy was employed to confirm that the spectral properties and resonance peak at 800 nm were preserved after radiolabeling, ensuring the nanoconjugates maintained their optimal optical characteristics for potential photothermal applications.

Quality control and stability of ^{99m}Tc-GGS-PVP nanoconjugates

Prior to radiolabeling experiments, comprehensive quality control measures were implemented for the ^{99m}Tc eluate. For each elution from the ^{99}Mo /^{99m}Tc generator, critical parameters including radiolabeling yield, molybdenum breakthrough, aluminum breakthrough, and expiration time were carefully evaluated. To maintain optimal radiotracer quality, the expiration time was strictly limited to a maximum of 12 hours post-elution [21].

The radiochemical stability of the synthesized ^{99m}Tc-GGS-PVP nanoconjugates was systematically assessed in both RPMI medium and human serum at multiple time points (1, 2, 4, 12, and 24 hours). The evaluation was conducted using instant thin-layer chromatography (ITLC) with silica gel strips as the stationary phase and normal saline and methanol solution as the mobile phases. This chromatographic method effectively quantified the percentage of unbound ^{99m}Tc, providing crucial information about the in vitro stability of the radiolabeled nanoparticles under physiologically relevant conditions. Radioactivity distribution on the ITLC strips was precisely measured using a calibrated dose calibrator (CRC-15R, Capintec, France), allowing for accurate determination of radiochemical purity over time.

Cell culture

The CT26 murine colon carcinoma cell line was obtained from Pasteur Institute (Tehran, Iran) and maintained under standard culture conditions. Cells were cultured in RPMI-1640 medium (Gibco, Life Technologies Corp., USA) supplemented with 10% (v/v) fetal bovine serum (FBS) and antibiotics (100 units/mL penicillin and 100 µg/mL streptomycin) to prevent microbial contamination. The cultures were incubated at 37°C in a humidified atmosphere containing 5% CO_2 (NU 8500, NuAire Corp., USA) to ensure optimal growth conditions. Upon reaching 80-90% confluence as a monolayer, cells were harvested using 0.05% trypsin-EDTA solution for detachment. Cell viability and concentration were quantitatively assessed using the trypan blue exclusion method with a hemocytometer, ensuring consistent cell numbers and viability for subsequent experiments. This standardized cell culture protocol maintained the morphological and functional characteristics of the CT26 cells throughout the experimental procedures.

Cytotoxicity Assessment

The potential cytotoxic effects of GGS nanoparticles on CT26 cells were systematically evaluated using a concentration-dependent approach. Cells were seeded in 96-well plates at a density of 1×10^6 cells per well in 100 µL RPMI medium and allowed to adhere and stabilize for 24 hours in an incubator. Following this equilibration period, the culture medium was carefully aspirated and replaced with 100 µL fresh RPMI containing varying concentrations of GGS nanoparticles (0, 62.5, 125, 250, and 375 μmol) and for ^{99m}Tc at any concentration (0.2, 0.5,1,1.5, 2 mCi).

Notably, ^{99m}Tc exhibited no detectable cytotoxicity across all tested radioactivity levels [21]. The ^{99m}Tc-GGS-PVP nanoconjugate formulation selected for subsequent experiments possessed an activity concentration of 0.2 mCi/mL and a GGS nanoparticle concentration of 125 μmol [22].

Cellular Uptake and Retention Kinetics of ^{99m}Tc-GGS-PVP

Following the cytotoxicity assessment, we investigated the cellular uptake and retention kinetics of ^{99m}Tc-GGS-PVP nanoconjugate in CT26 colon cancer cells using the optimal concentration of 125 μmol, which considered less than 25% cytotoxicity. Four T-75 culture flasks were prepared, each containing 1×10^6 CT26 cells in complete growth medium. After cells reached appropriate confluence, 1 mL of ^{99m}Tc-GGS-PVP (containing 0.2 mCi radioactivity and 125 μmol GGS nanoparticle concentration) was added to each flask.

The time-dependent cellular association of the radiolabeled nanoparticles was evaluated at four distinct time points (2, 4, 20, and 24 hours post-incubation) to establish a comprehensive uptake profile. At each designated time point, the culture medium was carefully aspirated, and cells were harvested following standard trypsinization protocols. The cell suspension was centrifuged to separate the cellular fraction from the supernatant. Radioactivity in both the cell pellet and supernatant fractions was quantified using a calibrated dose calibrator.

The cellular uptake efficiency was calculated as the percentage of the administered radioactivity associated with the cellular fraction. Additionally, the retention kinetics were determined by monitoring the cellular

radioactivity over time. This experimental design allowed for precise evaluation of both the targeting efficiency and intracellular stability of the ^{99m}Tc-GGS-PVP nanoconjugates. All experiments were performed in triplicate to ensure statistical robustness and reproducibility of the results, providing valuable insights into the potential of these nanoparticles as theranostic agents for targeted cancer therapy.

In Vivo Biodistribution Analysis

Animal experiments were conducted in strict accordance with the NIH Animal Use and Care Guidelines and received approval from the Institutional Animal Care Committee of Mashhad University of Medical Sciences. To evaluate the in vivo biodistribution pattern of ^{99m}Tc-GGS-PVP nanoconjugates, a comprehensive time-course study was performed using BALB/c mice.

The experimental design included three groups of BALB/c mice (n=5 per group), aged 6–8 weeks and weighting 20–25 g, each designated for analysis at specific time points. The radiolabeled nanoparticles (^{99m}Tc-GGS-PVP) were administered via lateral tail vein injection to ensure systemic distribution. For the 1-hour and 4-hour groups, an average activity of 120 μCi was administered per mouse, while the 24-hour group received a higher dose of 240 μCi to compensate for radioactive decay and ensure adequate counting statistics at this extended time point. To establish the temporal biodistribution profile, separate groups of mice were humanely sacrificed at 1, 4, and 24 hours post-injection.

These specific time points were strategically selected to capture the complete pharmacokinetic profile: the 1-hour time point reveals initial distribution patterns and rapid organ uptake; the 4-hour measurement demonstrates intermediate-phase distribution and early metabolic processes; while the extended time points (24 hours) provide critical information about long-term retention, clearance pathways, and stability of the radiolabeled nanoparticles in circulation—particularly important given the 6-hour half-life of ^{99m}Tc and the potential theranostic applications of these nanoconjugates.

Following euthanasia, blood samples were collected, and multiple organs of interest were carefully excised, including intestine, heart, lungs, spleen, kidneys, liver, blood, bone, tail, and thyroid. Each tissue sample was precisely weighed and its associated radioactivity was measured using a calibrated well gamma counter (Delshid, DL100). The biodistribution data were quantitatively expressed as percent injected dose per gram of tissue (%ID/g), calculated by normalizing the measured radioactivity in each organ to its corresponding weight and the total injected dose. (Equation 1)

$$ID/g\,(\%) = \frac{CPM_{tissue}}{weight_{tissue}(g) * CPM_{injection}} * 100 \qquad (1)$$

Where CPM_{tissue} , $CPM_{injection}$ represent the counts per minute measured in the tissue sample and the injection dose (calculated as the difference between pre- and post-injection syringe measurements), respectively. This standardized approach provided valuable insights into the pharmacokinetics, tissue tropism, and elimination pathways of the ^{99m}Tc-GGS-PVP nanoconjugates, essential parameters for assessing their potential as theranostic agents for targeted cancer applications.

Results

^{99m}Tc-GGS*-PVP *Characterization

Figure 1A presents the particle size analysis (PSA) diagram obtained through dynamic light scattering (DLS), revealing a prominent peak at 4.4 nm for the bare GGS nanoparticles. The polydispersity index (PDI) was calculated as 0.33, indicating moderate heterogeneity in the particle size distribution. UV-Vis spectroscopic analysis of the synthesized samples confirmed the successful formation of GGS nanoshells, evidenced by a strong absorption band at 790 nm in the near-infrared (NIR) region and a weaker absorption band at 525 nm in the visible spectrum. Figure 1B illustrates the comparative absorption spectra of GGS-PVP and ^{99m}Tc-GGS-PVP in aqueous solution. While the unmodified GGS-PVP exhibited a strong absorption band at 790 nm, the ^{99m}Tc-labeled counterparts displayed characteristic absorption peaks at 790 nm (sample 6), 857 nm (sample 7), and 848 nm (sample 8), indicating successful radiolabeling with minimal alteration to the core optical properties. The particle size distribution analysis, determined by DLS, revealed a significant increase in the average particle diameter and PDI from 4.4 nm, 0.33 for bare GGS-PVP to 65.9 nm, and 0.41 for ^{99m}Tc-GGS-PVP (Figure 2). This dimensional increase of approximately 60.1 nm suggests the successful formation of a ^{99m}Tc molecular coating around the gold/gold sulfide nanoparticle core.

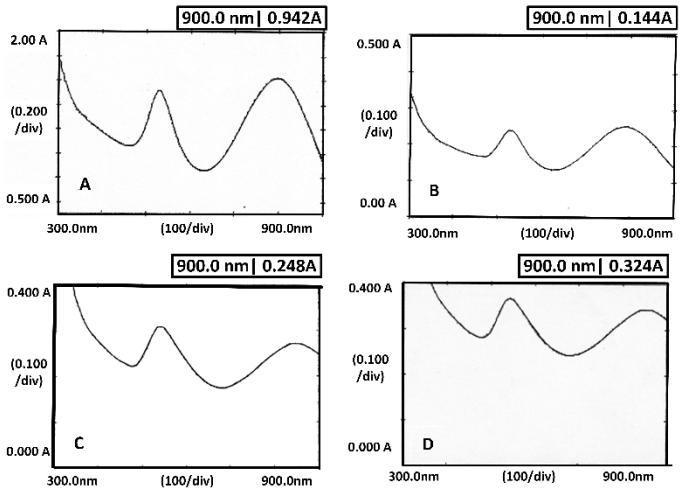

Figure1. A) Absorption spectra of GGS-PVP B) Absorption spectra of ^{99m}Tc-GGS-PVP; number 6 (peak 525, 790nm 0.59 mci activity), C) ^{99m}Tc-GGS-PVP; number 7(peak 545, 857nm 1.030 mci activity), D) ^{99m}Tc-GGS-PVP; number 8(peak 542, 848 nm 0.901 mci activity)

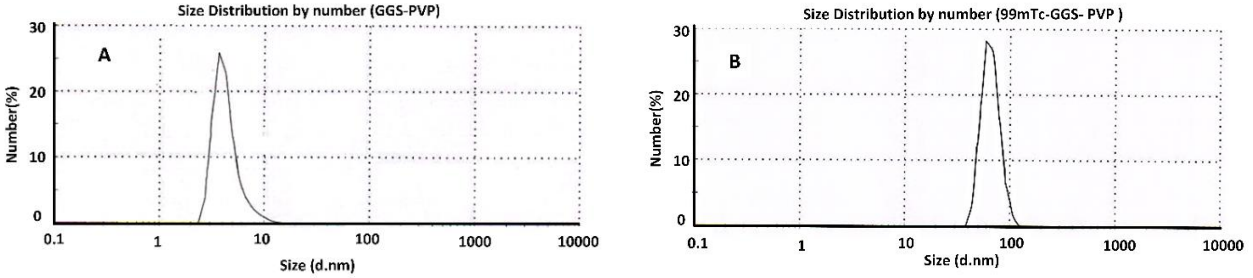

Figure 2) A) Size distribution of GGS-PVP (maximum abundance of particles distribution at 4.4 nm). B): Size distribution of synthesized ^{99m}Tc-GGS- PVP (maximum abundance of particles distribution at 65.9 nm.

Quality control and Stability of ^{99m}Tc-GGS-PVP Nanoconjugates

The labeling of GGS-PVP nanoparticles with technetium-99m (^{99m}Tc) was achieved with high efficiency and reproducibility. The radionuclide yield for ^{99}Mo was measured at 0.09 μCi. Radiochemical purity of the ^{99m}Tc -GGS-PVP nanoconjugates was determined to be 97.1 ± 1.1%, indicating successful labeling. No aggregation was observed in the labeled conjugates when suspended in distilled water, suggesting good colloidal stability post-radiolabeling. Size-exclusion chromatography demonstrated that the elution fractions corresponding to tubes 6–9 contained ^{99m}Tc -GGS-PVP nanoconjugates, while tubes 11–15 primarily contained free ^{99m}Tc, as illustrated in Figure 3.

The in vitro stability of the purified ^{99m}Tc-GGS-PVP nanoconjugates, summarized in Figure 4, was assessed over a 24-hour period in various media, with each experiment conducted in triplicate to ensure reproducibility. The nanoconjugates demonstrated high overall stability, particularly when methanol was utilized as the ITLC mobile phase. For instance, the radiochemical purity of ^{99m}Tc-GGS-PVP in methanol (Nanoconjugate/M) remained high at 95% after 24 hours, compared to 92% when assessed with normal saline (Nanoconjugate/NS). This superior stability with methanol was consistently observed across biological media as well: in RPMI, the purity at 24 hours was 85% with methanol versus 73% with normal saline, and in human serum, it was 82% with methanol compared to 74% with normal saline. These findings underscore the greater apparent stability of the nanoconjugates when methanol is used as the mobile phase, and suggest that normal saline provides a more rigorous test of radiolabel integrity, likely due to increased dissociation of weakly bound ^{99m}Tc.

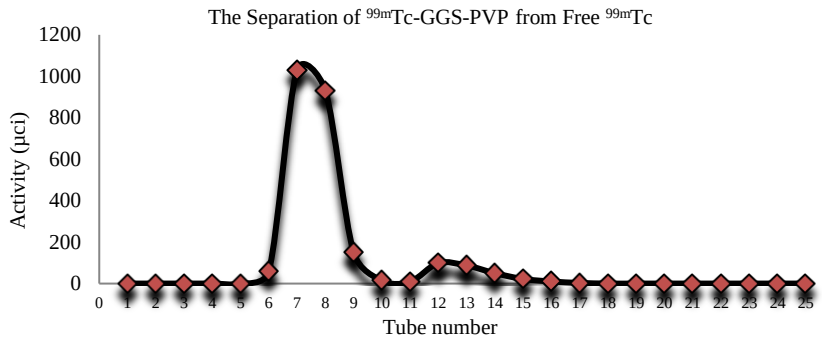

Figure 3. Purification profile of ^{99m}Tc-GGS-PVP nanoconjugates using Sephadex G-25 column chromatography. Elution fractions collected in tubes 6–9 correspond to ^{99m}Tc-labeled GGS-PVP nanoparticles, while fractions in tubes 11–15 represent free, unbound ^{99m}Tc.

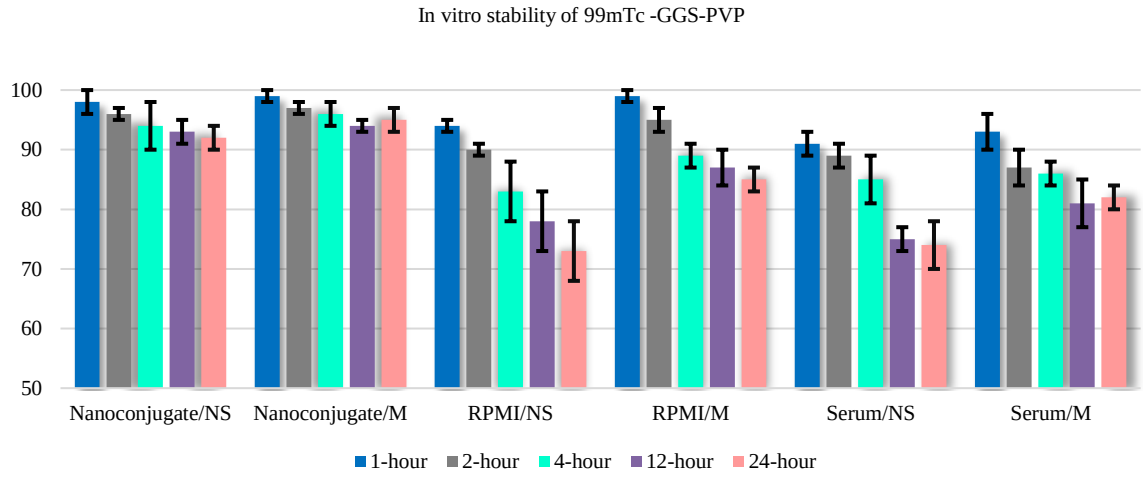

Figure 4. In vitro stability profile of ^{99m}Tc -GGS-PVP formulations after incubation at 37 °C for 1, 2, 4, 12, and 24 hours in 10 mL of fresh human serum, RPMI-1640 medium, and control (alone). Stability was assessed using instant thin-layer chromatography (ITLC) with two different mobile phases: normal saline (NS) and methanol (M).

In-vitro cytotoxicity assessment and Biodistribution

The cytotoxicity of ^{99m}Tc-GGS-PVP, GGS-PVP, and ^{99m}Tc eluted with distilled water on CT26 colon carcinoma cells was evaluated using the MTT assay. The dose-response curves for GGS-PVP and ^{99m}Tc-GGS-PVP nanoconjugate were evaluated. Free technetium-99m (up to 1 mCi) showed no cytotoxicity (>98% cell survival). However, both nanoparticle formulations exhibited concentration-dependent toxicity, with GGS-PVP (IC_{50} = 118.3 μmol) being more cytotoxic than its radiolabeled counterpart, ^{99m}Tc-GGS-PVP (IC_{50}=325.7 μmol). Figure 5 presents both sigmoidal and polynomial (3rd order) fits for the dose-response curves of GGS-PVP and ^{99m}Tc-GGS-PVP nanoparticles. For GGS-PVP, the sigmoidal model yielded an R^2 of 0.9331, slightly outperforming the polynomial fit with an R^2 of 0.9304. For ^{99m}Tc-GGS-PVP, both models provided an identical R^2 value, indicating a comparable statistical fit to the observed data. (R^2=0.996) Despite the close statistical performance, the sigmoidal model was consistently preferred for its inherent biological interpretability. This suggests that technetium-99m labeling alters the nanoparticle's biological interactions.

Based on the viability results, a concentration of 125 μmol for GGS and 200 μCi of ^{99m}Tc was selected for subsequent experiments (Figure 6). To evaluate the time-dependent binding of ^{99m}Tc-labeled GGS-PVP nanoconjugates to CT26 cells, a radiometric cell binding assay was performed. The radioactivity of both the medium (unbound fraction) and the harvested cells (bound fraction) was measured separately using a dose calibrator. The percentage of bound radioconjugates was calculated using the following formula (2):

$$Cell-bound\ activity\ (\%) = \frac{Radioactivity\ in\ cells}{Radioactivity\ in\ cells + Radioactivity\ in\ medium} * 100 \quad (2)$$

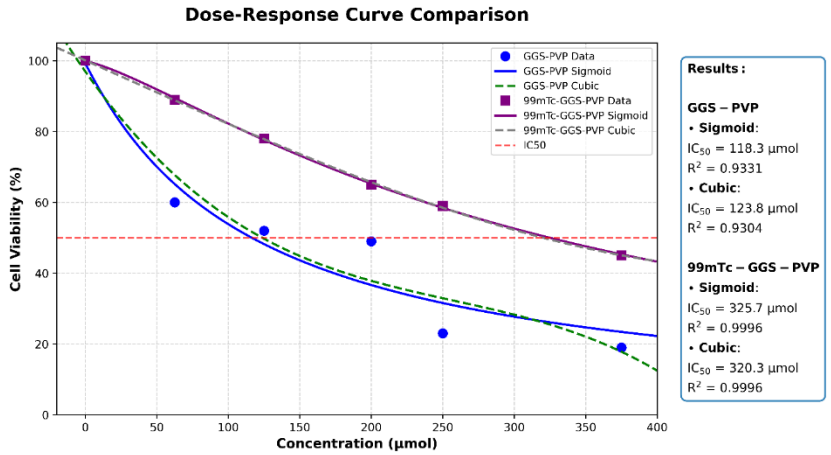

Figure 5. Dose-response curves of GGS-PVP and ^{99m}Tc-GGS-PVP nanoparticles. Experimental data (points) were fitted with sigmoidal (solid lines) and third-order polynomial (dashed lines) models. The red dashed line indicates 50% cell viability. The IC_{50} values and coefficient of determination (R^2) for each model are shown in the right panel. Results demonstrate differential cytotoxicity between the two nanoparticle formulations, likely due to the effect of technetium-99m radiolabeling.

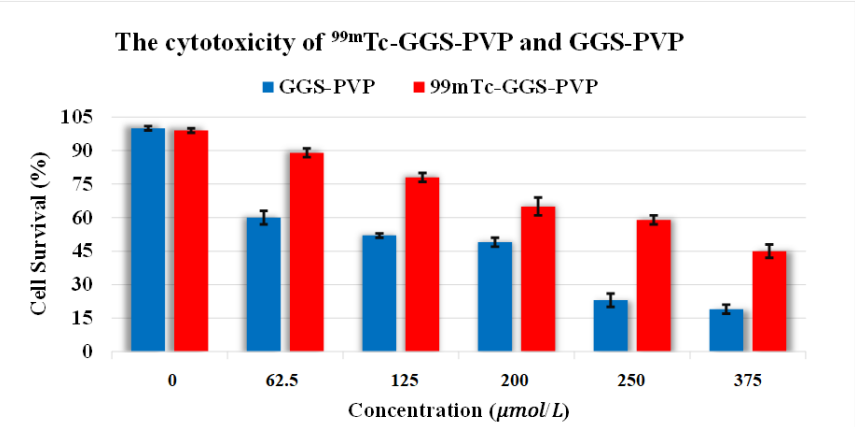

Figure 6. In vitro cytotoxicity assessment of ^{99m}Tc-GGS-PVP and GGS-PVP nanoparticles on CT26 colon carcinoma cells using the MTT assay. A concentration of 125 μmol GGS and 0.2 mCi ^{99m}Tc was selected for further studies.

Table1. Time-dependent cellular uptake of ^{99m}Tc-GGS-PVP nano conjugates in CT26 cells. Data shows progressive increase in cell-bound activity from 1.98% at 2 hours to 10.0% at 24 hours post-incubation (125 μmol GGS, initial activity 200 μCi).

Time (hour)	Total Activity in injection time (μCi)	Total Activity in test time (μCi)	Radioactivity in Medium (μCi)	Radioactivity in Cells (μCi)	Cell-bound Activity (%)
2	200	158.7	148±2	3±0.1	1.98
4	200	126.3	108±3	7±0.1	6.08
20	200	19.8	11±0.5	1±0.0	8.33
24	200	12.6	9±0.2	1±0.0	10.0

The binding data at different incubation times, summarized in Table 1, reveal a time-dependent interaction of ^{99m}Tc-GGS-PVP nanoconjugates with the cells. The percentage of cell-bound activity (relative to the total recovered radioactivity in the well) steadily increased throughout the 24-hour incubation period. This percentage rose from 1.98% at 2 hours to 6.08% at 4 hours, and further to 8.33% at 20 hours, culminating at 10.0% at 24 hours, indicating sustained cellular uptake or increasingly efficient binding of the nanoconjugates over time.

In-Vivo distribution

The in vivo biodistribution profile of ^{99m}Tc-GGS-PVP was evaluated in Balb/C mice at multiple time points (1, 4, and 24 hours) post-injection to assess tissue targeting and pharmacokinetic properties [23]. (Table 2)

Liver exhibited the highest accumulation of the radiolabeled nanoconjugates with 51.44 ± 7.54 %ID/g at one hour post-injection, followed by progressive clearance over time, consistent with hepatobiliary metabolism. Spleen uptake was considerably lower at 1.508 ± 0.81 %ID/g at one hour, also demonstrating a decreasing temporal pattern. The time-dependent reduction in hepatic and spleen retention suggests active metabolic processing and clearance of the ^{99m}Tc-GGS-PVP nanoconjugates from reticuloendothelial system organs.

Table 2. In vivo biodistribution of ^{99m}Tc-GGS-PVP in Balb/C mice (N=3 per group) expressed as percentage of injected dose per gram of tissue (%ID/g ± SD) at 1, 4, and 24 hours post-injection. Animals in the 1h and 4h groups received 120 µCi while the 24h group received 240 µCi to compensate for radioactive decay.

Tissue	1-hour	4-hour	24-hour
Intestine	0.492±0.040	0.567±0.247	0.461±0.221
Heart	0.230±0.040	0.411±0.289	0.900±0.377
Lungs	0.605±0.094	0.799±0.0732	0.755±0.218
Blood	0.388±0.0480	0.202±0.102	0.078±0.0113
Spleen	1.508±0.809	1.056±0.607	0.765±0.281
Kidneys	0.260±0.060	0.284±0.087	0.362±0.0553
Liver	51.444±7.544	35.071±2.679	14.191±6.541
Bone	0.203±0.050	0.299±0.183	0.303±0.250
Tail	0.379±0.171	7.741±10.42	1.693±1.3968
Thyroid	3.337±2.089	4.856±1.893	1.198±0.134

Thyroid uptake values of 3.337 ± 2.089 and 4.856 ± 1.893 %ID/g at 1 and 4 hours post-injection, respectively, indicated the presence of free ^{99m}Tc, highlighting the need for additional purification steps in the radiolabeling protocol. Notably, the relatively low renal uptake coupled with sustained hepatic retention demonstrates the remarkable stability of ^{99m}Tc-GGS-PVP in systemic circulation for up to 24 hours, a favorable characteristic for extended imaging and potential theranostic applications.

Discussion

This study successfully demonstrates the synthesis, characterization, and in vivo evaluation of ^{99m}Tc-labeled gold/gold sulfide nanoparticles coated with polyvinylpyrrolidone (^{99m}Tc-GGS-PVP) [24]. Our findings reveal several important aspects regarding the physicochemical properties, biological interactions, and biodistribution patterns of these nanoconjugates that have significant implications for their potential theranostic applications.

The successful synthesis of GGS-PVP nanoparticles was confirmed by UV-Vis spectroscopy, which revealed characteristic absorption peaks at 525 nm and 790 nm, consistent with previous reports on gold nanoshells [2, 3, 8, 25, 26]. The strong absorption band at 790 nm positions these nanoparticles as excellent candidates for NIR-mediated photothermal applications, as this wavelength falls within the optimal biological window (700-900 nm) for deep tissue penetration [1-3]. The substantial increase in particle diameter from 4.4 nm (bare GGS-PVP nanoparticles) to 65.9 nm (^{99m}Tc-GGS-PVP) can be attributed to several factors:

The ^{99m}Tc-stannous chloride complex incorporation into the nanoparticle structure adds to the hydrodynamic diameter, and the increase in PDI from 0.33 to 0.41 after radiolabeling indicates a degree of nanoparticle aggregation could have occurred during the labeling process. This aggregation can be attributed to: Cross-linking effects of the reducing agent ($SnCl_2$), changes in surface charge during the radiolabeling process, and potential bridging effects of ^{99m}Tc between nanoparticles. This size increase has important implications for biodistribution and tumor targeting. While the final particle size (65.9 nm) remains within the optimal range for the enhanced permeability and retention (EPR) effect (typically 30-200 nm) [27, 28], it explains our observed biodistribution pattern with predominant liver uptake (51.44 ± 7.54 %ID/g at 1 hour). This size is large enough to avoid rapid renal clearance while still allowing for sufficient circulation time and eventual hepatobiliary clearance, as demonstrated by the progressive reduction in liver retention over 24 hours. Future tumor-bearing models will be needed to evaluate how these size and morphology characteristics influence tumor accumulation via the EPR effect [29, 30].

The high radiochemical purity (97.1 ± 1.1%) achieved in our radiolabeling protocol demonstrates efficient conjugation of ^{99m}Tc to the GGS-PVP nanoparticles. A key innovation in our approach was the use of distilled water instead of conventional normal saline for ^{99m}Tc generator elution, which significantly enhanced labeling efficiency by reducing competing ions during the radiolabeling process. This methodological refinement, along with optimized reaction conditions, overcame many challenges typically associated with radiolabeling of inorganic nanoparticles. The preservation of NIR absorption peaks post-radiolabeling (observed at 790 nm, 857 nm, and 848 nm for samples 6, 7, and 8, respectively) confirms the retention of optical properties crucial for photothermal applications. Notably, sample 7, which exhibited the highest radioactivity (1.03 mCi), also displayed a shifted NIR peak at 857 nm, potentially indicating a higher degree of ^{99m}Tc conjugation influencing the nanoparticle's plasmon resonance. This overall stability suggests the potential for dual-modality applications combining nuclear imaging with photothermal therapy.

ITLC confirmed good overall stability for ^{99m}Tc-GGS-PVP, though normal saline as the mobile phase consistently yielded lower radiochemical purities and thus higher free ^{99m}Tc than methanol as the mobile phase, particularly in biological media. This is likely because the higher ionic strength and aqueous nature of normal saline compete with the nanoparticle's surface ligands, facilitating the dissociation of weakly bound ^{99m}Tc, whereas methanol, with its lower ionic strength and different polarity, is less disruptive to the

coordination bonds, resulting in a higher apparent stability [2].

Intriguingly, the cytotoxicity data from the MTT assay reveals that the radiolabeling process with ^{99m}Tc significantly attenuated the inherent toxicity of GGS-PVP nanoparticles, resulting in markedly improved cell viability for ^{99m}Tc-GGS-PVP across all tested concentrations. This observation can be attributed to an increase in nanoparticle size and/or a change in their morphology upon radiolabeling, which subsequently leads to reduced cellular internalization and thus a modified biological response [1, 3, 31-33]. The time-dependent cellular uptake of ^{99m}Tc-GGS-PVP, increasing from 1.98% at 2 hours to 10.0% at 24 hours, suggests a gradual internalization process, likely through endocytosis [34-36].

This progressive uptake pattern is advantageous for theranostic applications, as it allows sufficient time for diagnostic imaging followed by potential therapeutic interventions. The moderate uptake level (10% at 24 hours) indicates that surface modifications with targeting moieties might be beneficial for enhancing cellular internalization in future developments, similar to the approach taken by Day et al. [1] with anti-HER2 antibody conjugation. However, for therapeutic modalities like photothermal therapy, where higher intra tumoral concentrations are crucial for efficacy, this level is likely suboptimal. Consequently, to fully realize the therapeutic potential and enhance specificity, active targeting strategies, such as conjugation with specific antibodies, are not merely beneficial but appear necessary for significantly increasing cellular internalization and improving the overall therapeutic index. This will be a key focus for future optimization.

Our findings on the biodistribution of ^{99m}Tc-GGS-PVP nanoconjugates align with previous studies on gold nanoparticles of similar size ranges. For instance, Kozics et al. [23] also reported primary accumulation of PEGylated gold nanoparticles in the liver and spleen of rats, highlighting a common biodistribution pattern mediated by the reticuloendothelial system.

The in vivo biodistribution profile of ^{99m}Tc-GGS-PVP nanoconjugates revealed a dynamic and favorable pattern, crucial for prospective theranostic applications. Initial, predominant hepatic accumulation (approximately 51 %ID/g at 1 hour), characteristic of nanoparticles within this size range processed by the hepatobiliary system, was followed by substantial and progressive clearance over 24 hours (to ~14 %ID/g). This efficient hepatic washout is highly encouraging, suggesting effective metabolic processing and a diminished risk of long-term hepatotoxicity. Furthermore, the efficacy of the PVP coating in mitigating reticuloendothelial system (RES) uptake was evidenced by the markedly lower splenic accumulation (around 1.5 %ID/g at 1 hour) compared to the liver, a significant deviation from uncoated gold nanoparticles. The blood clearance kinetics (decreasing to ~0.08 %ID/g by 24 hours) indicated a circulating half-life conducive to facilitating tumor targeting via the enhanced permeability and retention (EPR) effect, while ensuring eventual systemic elimination. While transient thyroid uptake (peaking at ~4.9 %ID/g at 4 hours before declining to ~1.2 %ID/g by 24 hours) pointed to the presence of a minor fraction of free ^{99m}Tc initially, its effective clearance, coupled with minimal renal excretion (confirming the nanoparticles exceeded the renal filtration threshold), underscored the overall in vivo stability and integrity of the ^{99m}Tc-GGS-PVP nanoconjugates. Collectively, these findings highlight a promising biodistribution advantageous for both diagnostic imaging and targeted therapeutic interventions.

Despite the positive findings, key limitations include the small sample size in the biodistribution studies, the absence of an in vivo assessment of tumor-targeting efficacy, and a lack of investigation into the photothermal therapeutic potential. In addition, although hepatic uptake decreased markedly from 51.44 ± 7.54 %ID/g at 1 h to 14.19 ± 6.54 %ID/g at 24 h, indicating progressive clearance, the potential for long-term retention in the liver warrants further evaluation. Future research will therefore focus on validation in tumor-bearing animal and human cancer models to assess targeting efficiency, evaluation of photothermal capabilities under clinically relevant NIR irradiation, optimization with targeting ligands such as monoclonal antibodies or peptides to enhance cellular uptake, and comprehensive long-term biodistribution and toxicity studies , including detailed investigation of changes in nanoconjugate shape, and surface charge for a more precise evaluation of their impact on toxicity and cellular interactions, to address safety concerns prior to clinical translation.

Conclusion

This study successfully demonstrates the development of ^{99m}Tc-labeled GGS-PVP nanoconjugates with favorable physicochemical properties, excellent in vitro stability, and predictable in vivo biodistribution patterns. The predominant hepatic clearance pathway, moderate blood circulation time, and minimal cytotoxicity support the potential of these nanoconjugates as safe diagnostic agents. The preservation of NIR absorption properties after radiolabeling further highlights their potential as dual-modality theranostic platforms, combining nuclear imaging with photothermal therapy capabilities. While further optimization and in vivo efficacy studies are warranted, ^{99m}Tc-GGS-PVP nanoconjugates represent a promising advancement in the field of nanoparticle-based cancer theranostics.

Acknowledgment

The authors declare that they have no known competing financial interests or personal relationships that could have appeared to influence the work reported in this paper.

References

1. Day ES, Bickford LR, Slater JH, Riggall NS, Drezek RA, West JL. Antibody-conjugated gold-gold sulfide nanoparticles as multifunctional agents for imaging and therapy of breast cancer. International journal of nanomedicine. 2010:445-54.
2. Gobin AM, Watkins EM, Quevedo E, Colvin VL, West JL. Near-infrared-resonant gold/gold sulfide nanoparticles as a photothermal cancer therapeutic agent. Small. 2010;6(6):745-52.
3. Ramezanzadeh E, Sadri K, Momennezhad M, Dolat E, Sazgarnia A. Evaluation of EGFR-targeted gold/gold sulfide (GGS) nanoparticles as a theranostic agent in photothermal therapy. Materials Research Express. 2018;5(12):125401.
4. Sadat-Darbandi M, Fathabadi A, Oloomi S, Sazgarnia A. Dual-Modality Therapy: Synergistic Enhancement of Radio-Hyperthermia by Gold-Gold Sulfide Nanoparticles in MCF-7 Cells. Avicenna Journal of Medical Biotechnology. 2025;17(4):303-11.
5. Vines JB, Yoon J-H, Ryu N-E, Lim D-J, Park H. Gold nanoparticles for photothermal cancer therapy. Frontiers in chemistry. 2019;7:167.
6. Li R, Tu W, Wang H, Dai Z. Near-infrared light excited and localized surface plasmon resonance-enhanced photoelectrochemical biosensing platform for cell analysis. Analytical chemistry. 2018;90(15):9403-9.
7. Rahaman M, Moras S, He L, Madeira TI, Zahn DR. Fine-tuning of localized surface plasmon resonance of metal nanostructures from near-Infrared to blue prepared by nanosphere lithography. Journal of Applied Physics. 2020;128(23).
8. Demir M, Çizmeciyan MN, Sipahioğlu D, Khoshzaban A, Ünlü MB, Acar HY. Portfolio of colloidally stable gold–gold sulfide nanoparticles and their use in broad-band photoacoustic imaging. Nanoscale. 2025;17(3):1371-80.
9. Sadat-Darbandi M, Fathabadi A, Oloomi S, Sazgarnia A. Dual-Modality Therapy: Synergistic Enhancement of Radio-Hyperthermia by Gold-Gold Sulfide Nanoparticles in Mcf-7 Cells. Available at SSRN 4905801.
10. Nejabat M, Samie A, Ramezani M, Alibolandi M, Abnous K, Taghdisi SM. An overview on gold nanorods as versatile nanoparticles in cancer therapy. Journal of Controlled Release. 2023;354:221-42.
11. Wang Y, Gao Z, Han Z, Liu Y, Yang H, Akkin T, et al. Aggregation affects optical properties and photothermal heating of gold nanospheres. Scientific reports. 2021;11(1):898.
12. Gao W, Fan X, Bi Y, Zhou Z, Yuan Y. Preparation of NIR-responsive gold nanocages as efficient carrier for controlling release of EGCG in anticancer application. Frontiers in Chemistry. 2022;10:926002.
13. Murphy CJ, Chang H-H, Falagan-Lotsch P, Gole MT, Hofmann DM, Hoang KNL, et al. Virus-sized gold nanorods: Plasmonic particles for biology. Accounts of chemical research. 2019;52(8):2124-35.
14. Mochizuki C, Nakamura J, Nakamura M. Development of non-porous silica nanoparticles towards cancer photo-theranostics. Biomedicines. 2021;9(1):73.
15. Sun X, Zhang G, Patel D, Stephens D, Gobin AM. Targeted cancer therapy by immunoconjugated gold–gold sulfide nanoparticles using Protein G as a cofactor. Annals of biomedical engineering. 2012;40:2131-9.
16. Liu Y, Chorniak E, Odion R, Etienne W, Nair SK, Maccarini P, et al. Plasmonic gold nanostars for synergistic photoimmunotherapy to treat cancer. Nanophotonics. 2021;10(12):3295-302.
17. Guo Z, Zhu AT, Fang RH, Zhang L. Recent Developments in Nanoparticle-Based Photo-Immunotherapy for Cancer Treatment. Small methods. 2023;7(5):2300252.
18. Arulsudar N, Subramanian N, Mishra P, Sharma R, Murthy R. Preparation, characterisation and biodistribution of 99mTc-labeled liposome encapsulated cyclosporine. Journal of drug targeting. 2003;11(3):187-96.
19. Banihashem S, Nikpour Nezhati M, Panahi HA, Shakeri-Zadeh A. Synthesis of novel chitosan-g-PNVCL nanofibers coated with gold-gold sulfide nanoparticles for controlled release of cisplatin and treatment of MCF-7 breast cancer. International Journal of Polymeric Materials and Polymeric Biomaterials. 2020;69(18):1197-208.
20. Eshghi H, Attaran N, Sazgarnia A, Mirzaie N, Shanei A. Synthesis and characterisation of new designed protoporphyrin-stabilised gold nanoparticles for cancer cells nanotechnology-based targeting. International journal of nanotechnology. 2011;8(8-9):700-11.
21. Khorasanchi AR, Ramezanzadeh A, Eskandari A, Saatchian E, Yahyaei MR, Ramezanzadeh E. Evaluating Estimated Dose outside the Patients Undergoing Myocardial Perfusion Imaging with 99m Tc-MIBI. Iranian Journal of Medical Physics/Majallah-I Fīzīk-I Pizishkī-i Īrān. 2023;20(2).
22. Kamiloglu S, Sari G, Ozdal T, Capanoglu E. Guidelines for cell viability assays. Food frontiers. 2020;1(3):332-49.
23. Kozics K, Sramkova M, Kopecka K, Begerova P, Manova A, Krivosikova Z, et al. Pharmacokinetics, biodistribution, and biosafety of PEGylated gold nanoparticles in vivo. Nanomaterials. 2021;11(7):1702.
24. Abu-Dief AM, Alsehli M, Awaad A. A higher dose of PEGylated gold nanoparticles reduces the accelerated blood clearance phenomenon effect and induces spleen B lymphocytes in albino mice. Histochemistry and Cell Biology. 2022;157(6):641-56.
25. Sadeghi HR, Bahreyni-Toosi MH, Meybodi NT, Esmaily H, Soudmand S, Eshghi H, et al. Gold-gold sulfide nanoshell as a novel intensifier for anti-tumor effects of radiofrequency fields. Iranian Journal of Basic Medical Sciences. 2014;17(7):516.
26. Sadeghi HR, Toosi MHB, Soudmand S, Sadoughi HR, Sazgarnia A. Gold-Gold Sulfide nanoparticles intensify thermal effects of radio frequency electromagnetic field. Journal of Experimental Therapeutics & Oncology. 2013;10:285-91.
27. Xu L, Xu M, Sun X, Feliu N, Feng L, Parak WJ, et al. Quantitative comparison of gold nanoparticle delivery via the enhanced permeation and retention

(EPR) effect and mesenchymal stem cell (MSC)-based targeting. ACS nano. 2023;17(3):2039-52.
28. Gawali P, Saraswat A, Bhide S, Gupta S, Patel K. Human solid tumors and clinical relevance of the enhanced permeation and retention effect: a ʻgolden gateʻfor nanomedicine in preclinical studies? Nanomedicine. 2023;18(2):169-90.
29. Shinde VR, Revi N, Murugappan S, Singh SP, Rengan AK. Enhanced permeability and retention effect: A key facilitator for solid tumor targeting by nanoparticles. Photodiagnosis and Photodynamic Therapy. 2022;39:102915.
30. Kobayashi H, Watanabe R, Choyke PL. Improving conventional enhanced permeability and retention (EPR) effects; what is the appropriate target? Theranostics. 2013;4(1):81.
31. Patil T, Gambhir R, Vibhute A, Tiwari AP. Gold nanoparticles: synthesis methods, functionalization and biological applications. Journal of Cluster Science. 2023;34(2):705-25.
32. Cheng T-M, Chu H-Y, Huang H-M, Li Z-L, Chen C-Y, Shih Y-J, et al. Toxicologic concerns with current medical nanoparticles. International journal of molecular sciences. 2022;23(14):7597.
33. Haripriyaa M, Suthindhiran K. Pharmacokinetics of nanoparticles: current knowledge, future directions and its implications in drug delivery. Future Journal of Pharmaceutical Sciences. 2023;9(1):113.
34. Zhang W, Taheri-Ledari R, Ganjali F, Mirmohammadi SS, Qazi FS, Saeidirad M, et al. Effects of morphology and size of nanoscale drug carriers on cellular uptake and internalization process: a review. RSC advances. 2023;13(1):80-114.
35. Varma S, Dey S, Palanisamy D. Cellular uptake pathways of nanoparticles: process of endocytosis and factors affecting their fate. Current pharmaceutical biotechnology. 2022;23(5):679-706.
36. Cong VT, Houng JL, Kavallaris M, Chen X, Tilley RD, Gooding JJ. How can we use the endocytosis pathways to design nanoparticle drug-delivery vehicles to target cancer cells over healthy cells? Chemical Society reviews. 2022;51(17):7531-59.